Check for updates

Mechanism analysis of Au, Ru noble metal clusters modified on TiO$_2$ (101) to intensify overall photocatalytic water splitting

Libin Yang, [ID] *[a] Peng Gao, [ID] [a] Jinghao Lu, [ID] [a] Wei Guo, [ID] [a] Zhuang Zhuang,[b] Qingqing Wang, [ID] [a] Wenjing Li [ID] [a] and Zhiying Feng [ID] [a]

Accelerating the separation and migration of photo-carriers (electron–hole pairs) to improve the photo-quantum utilization efficiency in photocatalytic overall water splitting is highly desirable. Herein, the photo-deposition of Ru or Au noble metal clusters with superior electronic properties as a co-catalyst on the (101) facet of anatase TiO$_2$ and the mechanism of intensifying the photocatalysis have been investigated by calculation based density functional theory (DFT). As a result, the as-synthesized Ru/TiO$_2$ and Au/TiO$_2$ exhibit high hydrogen evolution reaction (HER) activity. Such a greatly enhanced HER is attributed to the interfacial interactivity of the catalysts due to the existence of robust chemical bonds (Ru–O–Ti, Au–O–Ti) as electron-traps that provide the photogenerated electrons. In addition, the formation of new degenerate energy levels due to the existence of Ru-4d and Au-5d electronic impurity states leads to the narrowing of the band gap of the catalysts. In addition, the as-synthesized Au/TiO$_2$ exhibits more faster HER rate than Ru/TiO$_2$, which is attributed to the effects of surface plasmon resonance (SPR) as a synergistic effect of plasmon-induced 'hot' electrons that enhance the harvesting of the final built-in electric field and promote the migration and separation of the photo-carriers, which efficiently facilitates hydrogen evolution from the photocatalytic overall water splitting reaction.

1. Introduction

As both global energy consumption and concerns over environmental contamination continue to increase, it is imperative to develop renewable energy resources that neither rely on fossil fuels nor emit carbon dioxide. Solar energy has attracted much interest as one such sustainable and clean energy. Further, it is very promising to use particulate semiconductors in photo-catalytic overall water splitting (OWS) to convert solar energy into clean and efficient hydrogen energy.[1–4] However, it should be noted that the absorption of sunlight by particulate semi-conductors is low and only 5% of the ultraviolet region of sunlight can be absorbed.[5] Furthermore, it is supposed that the future photocatalytic systems will have a solar-to-hydrogen (STH) conversion efficiency of 10%, which is far higher than the values currently obtained in small-scale trials that are typically about 1%.[6] To improve the utilization of solar energy, various particulate photocatalysts in overall water splitting and modified semiconductor materials have been investigated.[7–11] The main approach is to design the band structure, to control the migration of photo-carriers, and to intensify the surface reaction on the photocatalysts with suitable optical absorption, fast mobility of the photo-carriers, and efficient surface reaction, by compositional tuning and modified semiconductors, such as semiconductor coupling, ion doping or metal adsorption, and dye sensitization.[12–15] For example, Can Li *et al.* modified Pt/PdS co-catalysts on the surface of CdS and achieved a high apparent quantum yield (AQY) of 93% for the hydrogen evolution reaction.[16] Ag-based nanocomposites have been applied as photocatalysts with high activity, such as prepared Ag/g-C$_3$N$_4$ nanofibers that enhanced the separation capability of photoinduced electron–hole pairs.[17] Besides, iridium complexes have been explored as active photosensitizers (PSs) that increase the AQY due to the absorption of visible light, leading to charge-separation and long-lived excitation for hydrogen evolution reaction.[18–20] Despite this high AQY, the STH is only ∼1%, which is still far from reaching the minimum demand for industrialization. It is necessary to search for effective strategies to improve the STH efficiency of semiconductor-based catalysts.

In the photocatalytic OWS to produce hydrogen, the band structure of the semiconductor as the photocatalyst for sunlight absorption is critical. Titanium dioxide (TiO$_2$) is one kind of an important oxide that finds extensive application in the field of photocatalysis,[21,22] photovoltaics,[23,24] pigments,[25] and hydrogen production,[26–29] due to its favourable properties including non-

[a]College of Chemical Engineering and Materials Science, Tianjin Key Laboratory of Brine Chemical Engineering and Resource Eco-utilization, Tianjin University of Science and Technology, Tianjin 300457, China. E-mail: yanglibin@tust.edu.cn

[b]Institute of Coal Chemical Industry Technology, CHN Energy Ningxia Coal Industry Group Co. Ltd., Yinchuan, Ningxia 750411, China

toxicity, chemical stability, and low cost.[30–32] As mentioned before, the performance in the hydrogen evolution reaction depends on the band structure of TiO_2, which is a wide band-gap of 3.2 eV and 3.0 eV for anatase and rutile, respectively.[33] For hydrogen evolution, a wide band-gap semiconductor can only absorb ultraviolet (UV) radiation. In addition, the photo-carriers obtained from light radiation, *i.e.*, electrons (e^-) and holes (h^+) cannot rapidly migrate to the surface of TiO_2 for photocatalytic reaction and some electrons (e^-) and holes (h^+) recombine in the bulk. Furthermore, hydrogen evolution reaction (HER) on the surface of the semiconductor has been accompanied by oxygen reduction reaction (ORR), which is the reverse of the overall water splitting reaction. These are the three main reasons for the low efficiency of STH and AQY based on the TiO_2 photocatalysts. In order to overcome these short-comings, numerous attempts have been made with respect to change in the band structure of TiO_2, such as metal adsorption[34–36] and modification of the surface.[37]

The co-catalyst is important in integrated OWS systems as it provides active sites on the surface of the photocatalysts and protects the photocatalyst surface from being oxidized by the holes.[12] Co-catalyst components typically tend to overlap with the components of the electrocatalysts[38,39] and metal or metal oxide nanoparticles dispersed on the surface of the semiconductor particles are frequently used as co-catalysts.[34,40,41] In addition, composite material based co-catalyst are of great interest in many fields, such as HER, CO, and NO_x oxidation.[42] A typical example is the combination of Pt[43] and TiO_2, which is catalytically active and promotes H_2 evolution. The bifunctional effect on the alloyed interface sites of Cu-based bimetallic supported CeO_2 showed excellent activity including the Cu–Pt[44,45] and Cu–Rh[44] catalysts for CO oxidation. Graphene nanoplatelets were found to have eminent optical and electrical properties as co-catalysts,[46] such as graphene/g-C_3N_4 composites as photocatalyst that achieved AQY for HER.[47] The conversion efficiency of bimetallic Pt–Rh supported ceria–zirconia–alumina (CZA) reached near 100% for NO_x and CO oxidation.[48] The FeMnTiO$_x$-based co-catalyst with deposited tourmaline by the sol–gel method was highly efficient in NO oxidation.[49] The enhancement in the mechanical property of the *cis*-poly-butadiene nanocomposite was achieved by the addition of palygorskite nanofibers modified with the mercaptosilane coupling agent and HTPB.[50] However, this mechanism has not been deduced and these electro-catalysts are not directly applicable as OWS photocatalysts. It may be because the catalysts are usable in an irreversible electrolysis system but are not effective in the form of a particulate photocatalyst based on a reversible process.

In 2008, nano-silver was adsorbed on the surface of TiO_2 and significantly improved the photocatalytic degradation activity of TiO_2 under UV illumination.[51] Noble metals with surface plasmon resonance (SPR) effect (such as Au,[52] Ag[53]) were applied to photocatalysis. It was found that the introduced nano-gold could improve the hydrogen evolution under visible light irradiation when nano-gold and platinum were loaded on the surface of WO_3.[54] These works suggest that the enhanced mechanism of photocatalysis due to SPR effect is electromagnetic near field enhanced by metals that promote the migration of photo-carriers so as to benefit the photocatalytic reaction. Except for the SPR effect, the induced metals onto the semiconductor photocatalysts as the co-catalyst could aggregate the photogenerated electrons to inhibit the recombination of photogenerated carriers. The synergistic effect of the co-catalyst has not been indentified. Remarkably, it is noteworthy that the interaction of the metal–semiconductor not only helps to stabilize the fine adsorption of the nanometals on the semiconductor but also dramatically affects the electronic structures and optical properties of the semiconductor.[55]

In the present work, we prepared Au, Ru nano-clusters on the (101) facet of anatase TiO_2 as the co-catalyst and investigated the photocatalytic activity of overall water splitting. The enhancement mechanism of photocatalytic activity was analysed from the molecular scale by experiments and density functional theory (DFT) calculations.

2. Experimental section

2.1. Experimental details

2.1.1. Reagents. All the chemicals were analytical grade and used as received without further purification. Titanium butoxide ($C_{16}H_{36}O_4Ti$, ≥99%), gold chloride trihydrate ($HAuCl_4$, ≥99.9%), and ruthenium chloride hydrate ($RuCl_3 \cdot xH_2O$, 42% as Ru) were purchased from Aladdin, Shanghai, and were employed as Ti, Au, and Ru sources, respectively. Hydrochloric acid (HCl, 36.5%/wt%), sodium sulfate (Na_2SO_4), methanol (CH_4O, A.R.), and ethanol (C_2H_6O, A.R.) were supplied by Sinopharm Chemical Reagent Co., Ltd, Tianjin. Deionized water (DIW) was homemade.

2.1.2. Materials. In the present experiments, the anatase TiO_2 sample as the base photocatalyst was prepared according to the hydrothermal method.[56] The typical synthetic route includes hydrolysis and hydrothermal processes. Before the hydrothermal process, 60 mL of titanium butoxide was hydrolyzed by the dropwise addition of 8.2 mL hydrochloric acid (HCl, 36.5%/wt%). After stirring at room temperature for 16 h, a clear solution was obtained. Then, this was followed by transfer to a 100 mL Teflon-lined autoclave, after conducting a hydrothermal process at 180 °C for 36 h and allowing the reaction mixture to cool naturally to room temperature. Afterwards, the white product was separated by centrifugation at 10 000 rpm for 10 min and washing several times with a mixture of ethanol and deionized water. After that, the product was dried in air at 120 °C for 3 h.

2.1.3. Preparation of Au, Ru/TiO$_2$ photocatalyst. The synthetic strategy for the Au, Ru nanoparticles involved their deposition on the anatase TiO_2 photocatalyst by photo-reduction methods.[35] As given previously, the amount of adsorption is expressed by the weight of the adsorbate per weight of the photocatalyst. Briefly, in the photo-reduction route, the TiO_2 (1 g) powder was ultrasonically dispersed in 100 mL of 20 vol% aqueous methanol containing a definite amount of $HAuCl_4$ (10.46 mL, 0.956 mg mL^{-1}) or $RuCl_3$ (12.9 mL, 0.833 mg mL^{-1}) solution, and then the reduction of Au^{3+} or Ru^{3+} under irradiation of a xenon lamp (300 W) for 2 h was carried out, followed by washing with deionized water and drying in air at 120 °C for 3 h.

2.1.4. Photocatalytic reaction. The photocatalytic H_2 production reaction was carried out in a quartz glass reaction vessel. 0.1 g of the powdered photocatalyst was dispersed in 300 mL of H_2O solution and the solution was ultrasonically treated for 10 min. The temperature was maintained at room temperature by a flow of cool water during the photocatalytic reaction. The air in the reactor was completely displaced by the carrier gas and the reaction mixture was stirred. After this, irradiation by a Xe lamp (300 W) as the light source was carried out. The evolved mixture gases were detected with a BFRL 3420A gas chromatograph (equipped with a TCD detector and molecular sieve-5Å column) with argon (Ar) as the carrier gas. The conditions of temperature in the column (80 °C), injector (60 °C), and detector (120 °C) were preset.

2.1.5. Photoelectrochemical measurements. The photoelectrochemical measurements were carried out on an AUTO-LAB workstation (Biologic, SP300) in a three-electrode system, using photocatalyst-coated fluorine doped in a 1 cm × 1 cm FTO conductive glass substrate, platinum wire, and saturated Ag/AgCl electrode as the working, counter, and reference electrodes, respectively. For fabricating the working electrode, 10 mg of the photocatalyst was mixed with 1 mL ethanol, followed by at least 20 min ultrasonication with a homogeneous ink. Then, the suspension ink was spread on the FTO glass with an area of 1 cm^2 and the coated FTO was dried at 80 °C for 12 h. The measurement was performed at a constant potential of +0.6 V (vs. SCE) in 0.2 M Na_2SO_4 at room temperature. Linear sweep voltammograms (LSVs) were recorded at a scan rate of 1 mV s^{-1}. A 300 W Xe lamp was used as the light source.

2.1.6. Characterization of the catalysts. The crystallographic phases of the prepared samples were analysed by an X-ray diffractometer (XRD-6100, Shimadzu) operated at 36 kV, 30 mA using Cu Kα X-rays ($\lambda = 0.15405$ nm). The surface and microstructure of the as-synthesized products were examined by a field emission transmission electron microscope (FE-TEM/STM, JEO12100F) equipped with an energy dispersive X-ray spectrometer (EDS) operated at 200 kV. X-ray photoelectron spectroscopy (XPS, Thermo Fisher Scientific) was performed with a monochromatic Al Kα X-ray source. All the binding energies were compared against the C 1s peak of 284.4 eV as the internal standard. The Raman spectra were recorded with a dispersive microscope (HORIBA Jobin Yvon, HR-800). The UV-Vis diffuse reflectance absorbance spectra (DRS) were obtained with a UV-Vis-NTR spectrophotometer (UV-2550, Shimadzu) equipped with an integrated sphere and scanning in the range of 200–800 nm. The surface chemistry of the photocatalysts was analysed by Fourier transform infrared spectroscopy (FTIR, TENSOR27) in the transmission mode from 400 to 4000 cm^{-1}. Steady fluorescence emission spectra were recorded at room temperature with a fluorescence spectrophotometer (FLS1000, Edinburgh Instruments Ltd).

2.2. Computational methods and models

All the calculations of the molecular and electronic structures for the photocatalysts were based on density functional theory (DFT) with the exchange–correlation functional at the generalized gradient approximation (GGA) level parameterized by Perdew–Burke–Ernzerhof (PBE),[57] as implemented in the Cambridge Serial Total Energy Package (CASTEP) codes,[58] combined with ultrasoft pseudopotentials (USPP).[59] The calculations were converged at a cut-off energy of 400 eV for the plane wave basis set while the Brillouin zone (BZ) integrals were approximated using the special k-point girds with a mesh of 3 × 3 × 2 for geometry optimization and calculations of electronic properties, and the minimization algorithm was the Broyden–Fletcher–Goldfarb–Shanno (BFGS) scheme.[60] With a view to avoid the error of underestimating the band gap of the GGA method, the electronic structure calculations were conducted using the GGA + U method[46] in conjunction with GGA, which could produce a good band gap for TiO_2 in comparison with the experimental results.[61] In this research, the effective on-site coulombic interaction U for Ti-3d was set to 2.5 eV; it was verified that the calculated band gap of primitive TiO_2 is 3.2 eV, which is the same as the experimental value of 3.2 eV.[62] The convergence criteria for structure optimization and electronic properties were set as follows: (1) the maximal force on the atoms was 0.01 eV Å^{-1}; (2) the maximal atomic displacement was 2×10^{-3} Å; (3) the maximal energy change per atom was 2×10^{-5} eV.

The primitive structure of anatase TiO_2 was built according to a previous experimental work.[63] The facet (101) of anatase TiO_2 was simulated as a periodic (3 × 4) slab with a thickness of four O–Ti–O layers and with a 10 Å vacuum layer (Fig. 1). It has been proved that the periodic (3 × 4) slab is large enough to reduce the interactions between the neighbouring adsorbed metal clusters and to fully release the interfacial strain energy.[62] For geometry optimization of the A facet (101), the bottom two layers of the O–Ti–O atomic layers in the slab were constrained to their crystal lattice position but the upper two atomic layers were relaxed.

The structures of the adsorbed Ru or Au clusters on the anatase TiO_2 (101) facet were modelled and the optimized adsorption configurations are given in Fig. 2. In the adsorption configuration, ten of the Ru or Au atoms were adsorbed on the anatase TiO_2 (101) facet. Specifically, the configurations consist of three layers of adsorbed atoms. Seven atoms were adsorbed between four O_{2c} and three O_{3c}, Ti_{5c} on the interface of M (Ru or Au noble metal)/TiO_2 (101) facet and formed M–O, M–Ti bonds, which were attached to the bottom and sublayers of the interface. For the surface layer, the metal atoms were adsorbed on the metal atoms of the sublayers (shown in Fig. 2).
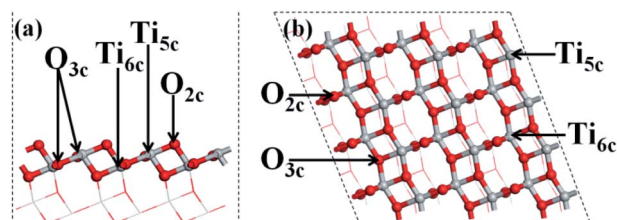

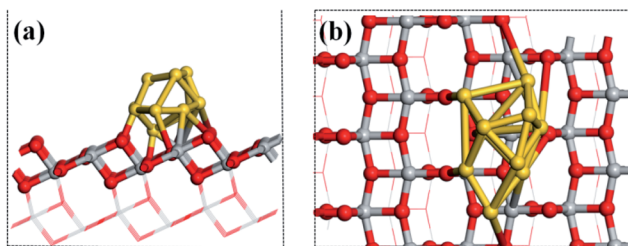**Fig. 1** Model of the structure. (a) Side and (b) top view of the (101) facet of anatase TiO_2.

Fig. 2 (a) Side and (b) top view of the structural model of the metal atoms adsorbed on TiO_2 (101). Gray, red, and gold spheres represent the Ti, O, and metal atoms, respectively.

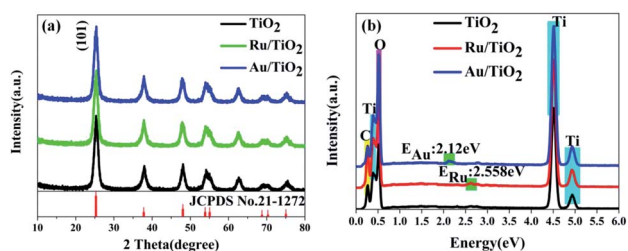Fig. 3 (a and b) XRD patterns and energy dispersive X-ray spectra (EDS).

Fig. 4 (a, b, and c) TEM images of the TiO_2, Ru/TiO_2, and Au/TiO_2 photocatalysts, respectively; (d, e, and f) HRTEM images of the TiO_2, Ru/TiO_2, and Au/TiO_2 photocatalysts, respectively.

3.   Results and discussion

3.1.   Microstructure characterization

The X-ray diffraction (XRD) patterns were recorded to ascertain the crystalline structure of all the samples. As is shown in Fig. 3a, the XRD patterns of the samples present the anatase phase, which has the cell parameters $a = b = 3.7852$ Å and $c = 9.5139$ Å corresponding to the space group D_{4h}^{19}-I_{41}/amd (JCPDS No. 21-1272). Furthermore, it must be mentioned that the diffraction of the strongest peak for the (101) facet indicates that the as-synthesized samples are present in pure anatase phase and predominantly the (101) facet. The crystallinity can be calculated from the integrated areas of the main peaks of the anatase facet (101); the average crystallite size, referred to as the crystal size, was calculated by the Scherrer equation.[64] The crystallite size and contribution of anatase was calculated to be about 8.3 nm and 84.18%, respectively (Table 1), based on the full width at half maximum and integrated areas of the (101) facet peaks. However, no clear peaks of Ru nanoparticles can be observed upon the adsorption of Ru nanoparticles on the (101)
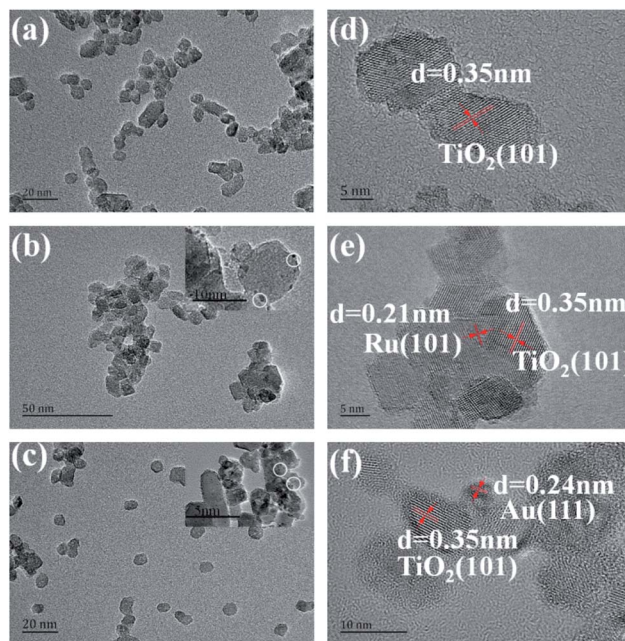
facet of anatase TiO_2. The absence of characteristic peaks for Ru may be attributed to the low content (0.71 wt%) (Table 1) and high-dispersion of the Ru flakes in the bulk of anatase TiO_2. A similar phenomenon was also observed for the Au/TiO_2 samples. Fig. 3b shows the energy dispersive X-ray spectroscopic (EDS) information for the Ru, Au energy peaks of the Ru, Au/TiO_2 samples, which further confirmed that the Ru, Au nanoparticles clusters were successfully synthesized by the photoreduction method.

The general morphology of Ru, Au/TiO_2 was also investigated by TEM measurements. As is shown in Fig. 4a–c, the as-synthesised Ru, Au/TiO_2 were globular catalysts with dark spots of Ru, Au nanoparticles. It was obvious that Ru or Au nanoparticles were dispersed on the (101) facet of TiO_2 (Fig. 4b and c) with a small size (10 nm), corresponding to the average crystallite size determined from the half peak width of the XRD patterns. HRTEM presented more details on the lattice fringes (0.35 nm), which match well with the XRD results of (101) facet of anatase TiO_2 (Fig. 4d). Ru, Au nanoparticles with 2 nm size can be found and their lattice fringes (0.21 nm and 0.24 nm,

Table 1 Crystalline properties, average crystallite sizes, and relative atomic ratio (wt%) of the as-synthesised samples determined from the XRD patterns and EDS, respectively

Samples	Crystalline contribution (wt%) Anatase	Amorphous contribution (wt%)	Average crystallite size (nm)	Relative atomic ratio (wt%)
TiO_2	84.18	15.82	7.9	0
Ru/TiO_2	83.93	16.07	8.3	0.707
Au/TiO_2	84.07	15.93	8.1	0.71

respectively, Fig. 4e and f) indicate that noble metal clusters were successfully adsorbed into the (101) facet from the HRTEM results, which are consistent with the EDS results (Fig. 4d).

3.2. Surface chemical structures

To detect the surface state of the as-synthesised photocatalysts, all the samples were analysed by FT-IR, XPS, and Raman spectroscopy. The strong absorption observed below 400–1003 cm^{-1} is attributed to the lattice vibrations of anatase TiO_2 and the bands at about 1600 cm^{-1} and 3340 cm^{-1} correspond to the O–H bending modes and stretching of water absorbed on the (101) facet of TiO_2, respectively (Fig. 5a). O–H absorbed on the (101) facet of TiO_2, which was favourable for absorbing the reduced noble metal particles, was partly preserved after heat treatment. As is shown in Fig. 5b, five phonon vibrations observed at 147.8, 200.02, 398.8, 518.75, and 643.56 cm^{-1} can be assigned to the E_g^1, E_{2g}^2, B_{1g}^1, $A_{1g} + B_{1g}^2$, and E_{3g}^3 stretching modes, respectively. Moreover, two slight shifts in the E_g^1 mode for higher wave-number (147.8 to 150.46, 151.9 cm^{-1}) were found for the Ru/TiO_2 and Au/TiO_2 samples, respectively (Fig. 5c), which illustrated that the adsorption of Ru or Au clusters forms a robust interaction between Ru or Au and anatase TiO_2. The existence of the robust interaction could be confirmed by the band at about 1404 and 1409 cm^{-1} observed for the Ru, Au/TiO_2 samples (Fig. 5a). Similar results were proved with the HRTEM results (Fig. 4e and f), indicating the formation of Ru–O–Ti or Au–O–Ti chemical bonds for the interaction between the Ru, Au samples and the (101) facet of anatase TiO_2.

As is shown in Fig. 6a, two main peaks were observed at the binding energies of 458.4 and 464.1 eV, corresponding to the Ti $2p_{3/2}$ and Ti $2p_{1/2}$ of the Ti^{4+} species, respectively. The energy separation between the Ti $2p_{3/2}$ and Ti $2p_{1/2}$ states is 5.7 eV, indicating the formation of the TiO_2 lattice. Besides, the oxygen species were also analysed from the O XPS spectra (Fig. 6b); the signal peak at the binding energy of 529.7 eV was assigned to the O 1s state of O^{2-} anion in the TiO_2 lattice.
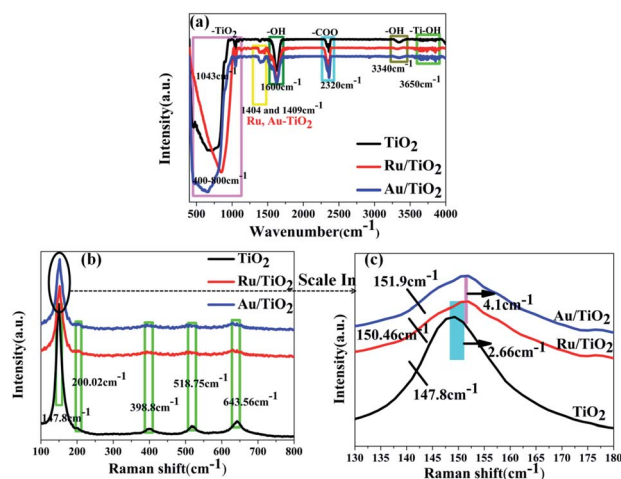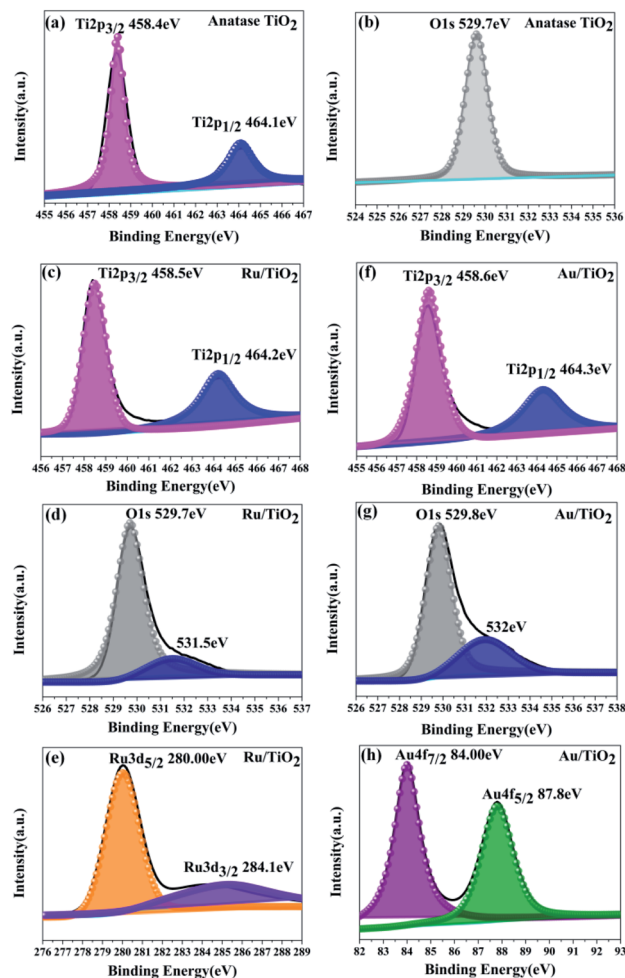

Fig. 6 XPS spectra for the Ti 2p, O 1s, Ru 3d, and Au 4f states of the anatase TiO_2 (a and b), Ru/TiO_2 (c–e), and Au/TiO_2 (f–h) photocatalysts, respectively.

Fig. 5 FTIR (a) and Raman (b and c) spectra of anatase TiO_2, Ru/TiO_2, and Au/TiO_2 photocatalysts, respectively.

Two main peaks for Ru/TiO_2 were observed, corresponding to the Ti $2p_{3/2}$ and Ti $2p_{1/2}$ core levels of the Ti^{4+} species, respectively, same as that in TiO_2. However, the binding energies of the Ti^{4+} species in the composite obviously shifted towards the higher end by about 0.1 eV (Ti $2p_{3/2}$ and Ti $2p_{1/2}$, respectively) as shown in Fig. 6c. Moreover, the binding energies of Ru $3d_{5/2}$ and Ru $3d_{3/2}$ were 280.1 and 284.2 eV, which are attributed to the Ru^0 and Ru^{3+} species, respectively. Comparing the Ru $3d_{5/2}$ (280.00 eV) peak with the Ru $3d_{3/2}$ (284.10 eV) peak in the samples, the binding energy shifted to the lower end by 0.10 eV (Fig. 6e) due to the electrons transferred to the centre of the d orbital of Ru from the Ti 2p orbital. The same result is also seen in Fig. 6d by the O 1s peak at the binding energy of 529.7 eV. However, a conspicuous peak was observed at the binding energy of 531.5 eV, which is assigned to the Ru–O bond (in Fig. 6d). As for the Au/TiO_2 photocatalyst, the O 1s peak at the binding energy of 529.8 eV shifted and increase by 0.1 eV. Importantly, the peak at 532 eV can be attributed to the Au–O bond (Fig. 6g). These bonding structures were observed in the Raman and FT-IR spectra (Fig. 5). Being similar to Ru/TiO_2, the binding energies of the Au $4f_{7/2}$ and Au $4f_{5/2}$ states were shifted

towards the lower values (Fig. 6h) due to the strong metal-carrier interaction aroused by the electron from the Ti 2p orbital to the Au orbital. Remarkably, a similar shift was also seen for Ti 2p (Fig. 6f). The enhancement in the blue-shift (lower direction) can be attributed to the electron transferred from the Ti 2p orbital to the Au orbital, which is due to surface plasmon resonance (SPR) of Au.

3.3. The interaction with electron-traps and local electric field

For semiconductors used in photocatalytic OWS, there are three mains steps as shown in Fig. 7. A semiconductor absorbs the photons with energies greater than its band gap, upon which the electrons in the semiconductor are excited from the valence band (VB) to the conduction band (CB). This generates electron–hole pairs as the initial step of the photocatalytic process (step 1). The electron–holes pairs are independently transferred to the surface of the semiconductor; meanwhile, the recombination of electron–hole pairs takes place in the bulk and on the surface of the semiconductors (step 2). Subsequently, they participate in the HER and OER on the surface of the photocatalysts (step 3). Thus, the improvement in the photo-quantum absorption efficiency and migration of the photo-induced electron–hole pairs in the photocatalytic hydrogen evolution from water splitting are highly desirable. Some active sites of the electron-traps were constructed on the surface of the specific (101) facet of TiO$_2$ to control the migration of photo-induced electron–hole pairs for inhibiting the recombination of the carriers.

As mentioned in the above results, the interfaces of Ru, Au/TiO$_2$ were observed in the HRTEM surface (Fig. 4e and f), which indicated the formed chemical bond as the strong interaction between the Ru, Au and the (101) facet of anatase TiO$_2$. In particular, the robust interaction of Ru–O–Ti or Au–O–Ti chemical bonds was formed after the Ru or Au cluster was adsorbed on the TiO$_2$ (101) facets, as proved by FT-IR, Raman spectroscopy, and XPS (Fig. 5 and 6).

To further investigate the interaction of Ru–O–Ti and the interface stability of Ru/TiO$_2$, the DFT method was adopted for simulation and analysis. The stability of the electronic

structures of M/TiO$_2$ (101) were estimated by the adsorption energy $E_{ads} = E_{atom/surface} - (E_{atom} + E_{surface})$. Here, E_{atom} is the energy of an isolated metal atom, $E_{surface}$ is the energy of the clean (101) surface slab, and $E_{atom/surface}$ is the total energy of the surface with metal atom (M) adsorption.[65] Table 2 reports the calculated adsorption energies for the Ru cluster-adsorbed facet (101) of anatase TiO$_2$. It was noted that the E_{ads} (Ru/TiO$_2$) was negative (−0.79 eV), indicating a favourable process and the steady adsorption of the Ru clusters onto the anatase TiO$_2$ (101) facets with chemical bonds. Thus, Ru cluster as the electron-trap was successfully constructed on the anatase TiO$_2$ (101) facets.

The effect of the electron-traps on activity enhancement of photocatalytic H$_2$ evolution in OWS, the interface electronic structure of electrostatic potential, and Mulliken charge were calculated based on DFT. The potential distribution can provide information about the electric field and transfer of the photogenerated charges in the photocatalytic systems. As reported in Table 2, the electrostatic potential of Ru/TiO$_2$ (101) (2.96 eV) was lower than that of the (101) facet of original TiO$_2$ (7.033 eV). The local final built-in electric field of the interface of the Ru/TiO$_2$ (101) structure pointed from the noble metal Ru layer of the TiO$_2$ (101) surface layer. In addition, the distribution of Mulliken charges can reveal the separated mechanism of carriers, as is shown in Table 2. The amount of electron transfer from the TiO$_2$ (101) layers to the Ru atoms layers is coincident with the XPS results (Fig. 6e). The differences in the electrostatic potential between the (101) facet of the original TiO$_2$ and Ru/TiO$_2$ may be due to the photogenerated electrons that tend to localize close to the adsorbed Ru clusters atoms, thus benefitting the separation of the photogenerated carriers. As is shown in Fig. 8a, the valence band (VB) and conduction band (CB) of TiO$_2$ were predominantly composed of O 2p states and Ti 3d states, respectively. As for the image showing the difference charge density (Fig. 8b), O atoms provide an electron rich region while Ti atoms provide a vacant orbital in the TiO$_2$ lattice. The DOS of Ru/TiO$_2$, as shown in Fig. 8c, illuminates the adsorbed Ru clusters that change the electronic properties of the original TiO$_2$. The electronic states of the Ru 4d impurity appeared at the top of the VB and the bottom of the CB, and exhibited some energy dispersion. Not surprisingly, the existence of the deletion region around the Ru clusters and its connection with the electron enrichment region of O atoms indicated the formation of the Ru–O chemical bond. The existence of electron enrichment region around the Ru clusters indicates that the transfer
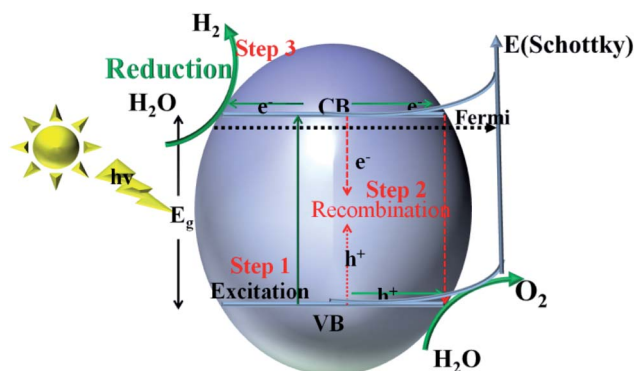
Fig. 7 Schematic illustration of the main processes within the photocatalytic overall water splitting reaction of semiconductors.

Table 2 The adsorption energy (E_{ads}), electrostatic potential, and the Mulliken charge for various configurations

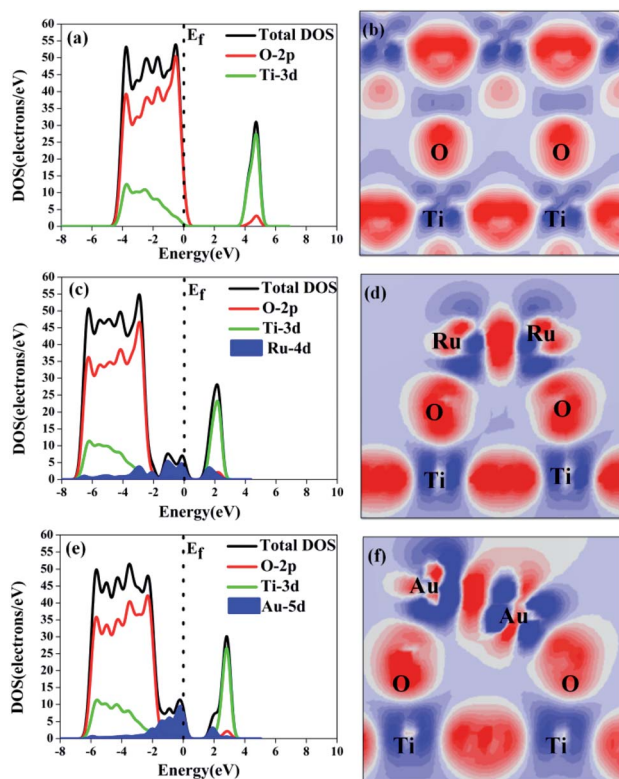| Configuration	E_{ads} (eV)	Electrostatic potential (eV)	Mulliken charge (e)
Free (101) facet	—	7.033	2.48
Ru/TiO$_2$ (101)	−0.79	2.96	2.72
Au/TiO$_2$ (101)	−0.85	2.23	2.87

Fig. 8 Density of states (a, c and e) and difference charge density (b, d and f) of the configuration model of anatase TiO$_2$, Ru/TiO$_2$, and Au/TiO$_2$, respectively. Red and blue represent electron enrichments and loss, respectively, and the brighter the colour, the more electrons are enriched or absent.

of the photoelectrons can be trapped to enrich the electrons (Fig. 8d).

The enhancement mechanism of the electron-traps for the photocatalytic overall water splitting is shown in Fig. 9. The generated electron would overcome the Schottky barrier and can be directly transfer to the surface of the electron-traps in the
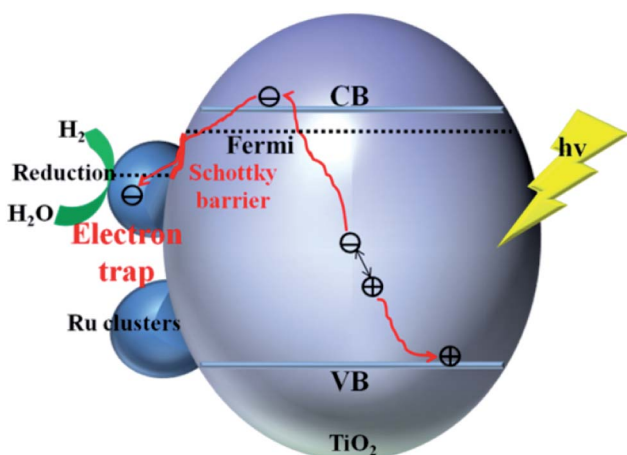

Fig. 9 Schematic illustration of the mechanism of electron-traps for the photocatalytic overall water splitting.

Ru clusters atoms owing to the existence of the local final built-in electric field of the interface of the Ru/TiO$_2$ (101) structure pointed from the noble metal Ru layer to the TiO$_2$ (101) surface layer. Further, the electron-traps formed on the surface of the (101) facet of TiO$_2$ by the introduction of noble metal Ru cluster collect the photogenerated electrons as the active sites for hydrogen evolution due to the existence of an electron enrichment region around the Ru clusters. Besides, due to the appearance of the Ru 4d electronic impurity states, a set of new degenerate energy levels are formed, thus narrowing the band gap and the promotion of electron migrated from the top of the Ru 4d electronic impurity state to the CB. Therefore, the electron-traps efficiently promoted the separation of the electron–hole pairs and provided active sites of the reduction reaction of photocatalytic splitting water upon the deposition of Ru nanoparticles on the (101) facet of TiO$_2$.

To investigate the effects of electron-traps on photocatalytic H$_2$ evolution, the optical responsiveness and degree of recombination of the photoelectron–hole pairs of the photocatalysts by diffuse reflectance UV-Vis (DRS), the Kubelka–Munk plots and steady-state fluorescence analysis were carried out. The diffuse reflectance UV-Vis spectra and Kubelka–Munk plots are presented in Fig. 10. The anatase TiO$_2$ nanoparticles exhibit an absorption edge at 387 nm and correspond to the band gap of 3.2 eV (Fig. 10b). Compared with the original TiO$_2$, the absorbance intensity of Ru/TiO$_2$ (101) in the visible region is significantly enhanced and corresponds to the band gap reduction of 2.98 eV. It is also proved that Ru/TiO$_2$ has a strong light response ability in the visible region. The steady-state fluorescence of TiO$_2$ shows an intense emission peak centred at about 443 nm under 380 nm excitation, which is attributed to the robust recombination of photo-carriers occupying the surface of TiO$_2$ (Fig. 11). The lower PL intensity for Ru/TiO$_2$ indicates that the visible light responses of Ru/TiO$_2$ can be enhanced by the absorbed Ru clusters. The quenching of the PL intensity of Ru/TiO$_2$ demonstrates that the Ru–O–Ti chemical bond can efficiently suppress the recombination of photogenerated carriers and promote the separation of the electron–hole pairs.

The photocatalytic hydrogen evolution performance of the as-prepared photocatalysts was measured. As is shown in Fig. 12a and b, compared with a negligible photocatalytic activity for H$_2$ evolution on the original TiO$_2$ particles, Ru/TiO$_2$ showed a powerful photocatalytic activity of about 40.78 μmol g^{-1} h^{-1}, which is greater by about two orders of magnitude.
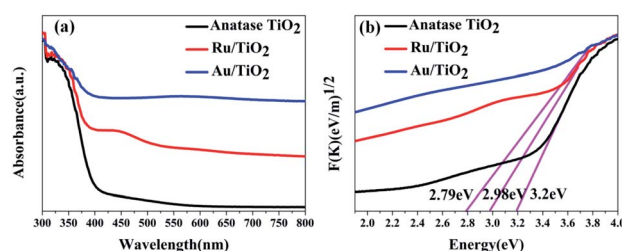

Fig. 10 UV-Vis absorbance spectra (a) and Kubelka–Munk plots of anatase TiO$_2$, Ru/TiO$_2$, and Au/TiO$_2$ photocatalysts (b), respectively.
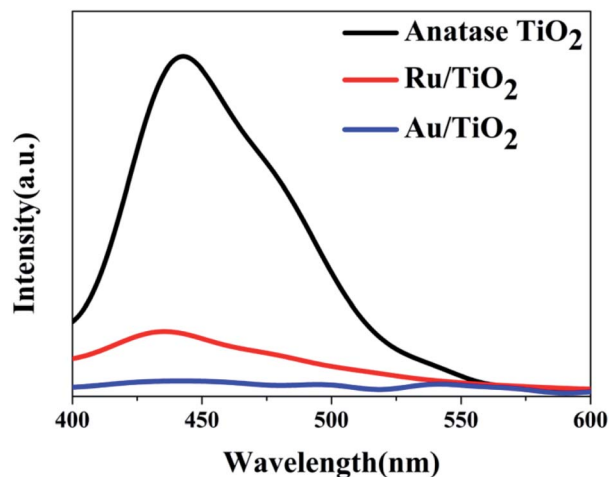
Fig. 11 The steady-state fluorescence spectra of anatase TiO_2, Ru/TiO_2, and Au/TiO_2 photocatalysts excited by 380 nm light, respectively.

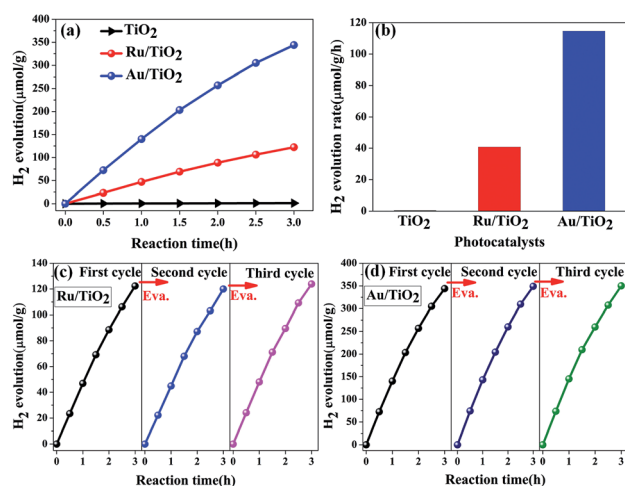Fig. 12 (a and b) Photocatalytic H_2 evolution reactions by various photocatalysts (anatase TiO_2, Ru/TiO_2, Au/TiO_2); (c and d) cycling test of photocatalytic H_2 evolution reactions for Ru/TiO_2 and Au/TiO_2, respectively. Reaction conditions: 100 mL pure water; catalyst amount, 100 mg; light source, xenon lamp (300 W); temperature, 25 °C.

Except for Ru induced as the co-catalyst that increases the absorption of light, the exposed active sites as the traps on the surface of basic TiO_2 effectively aggregate the photogenerated electrons for reduction reactions and efficiently suppress the recombination of electron–hole pairs upon deposition of Ru nanoparticles on the (101) facet of TiO_2. In addition, the stability of the Ru/TiO_2 photocatalysts were also cycle-tested (Fig. 12c). The amount and rate of H_2 evolution were constant after the third cycle, indicating that the photocatalysts are physically and chemically stable in the photocatalytic hydrogen evolution reaction.

Photoelectrochemical measurements were conducted to evaluate the separation of the photo-generated electrons of the photocatalysts. Aimed at demonstrating the role of the Ru

clusters in altering the separation of the electrons in Ru/TiO_2, the LSV scans and transient photocurrent responses were measured. Fig. 13a shows the LSV of TiO_2, Ru/TiO_2, and Au/TiO_2 electrodes in 0.2 M Na_2SO_4 solution under light irradiation. TiO_2 exhibited a negligible current, which is attributed to the robust recombination of photo-carriers that occupy the bulk and surface of TiO_2. Moreover, the photocurrent of Ru/TiO_2 is much higher than that of TiO_2, indicating that more electron carriers were produced from TiO_2 by assembling the surface of the Ru clusters. As shown in Fig. 13b, compared with TiO_2, significant photocurrent was observed for Ru/TiO_2 and Au/TiO_2 under dark conditions; the dark current could be attributed to the different carrier concentrations above the barrier level. Different from the low dark currents of the photocatalysts, as theirs are photosensitive, the photocurrents under the light were all higher than the dark currents. TiO_2 showed a weak photocurrent response, further confirming the existence of strong recombination of the photo-carriers. A significant photocurrent was observed for Ru/TiO_2, indicating low recombination of the photo-generated charge carriers. This could be attributed to the strong interaction and act as electron-traps due to the deposited Ru clusters, which can efficiently promote the rapid migration and separation of the photo-generated electron–hole pairs.

To demonstrate the enhancement activity of TiO_2 modified by noble metal clusters for photocatalytic hydrogen evolution except for the effect of electron-traps, the Au nanoclusters as the active sites with surface plasmon resonance (SPR) effect were simulated by DFT and proved by catalytic response results. Herein, SPR is a phenomenon of resonant oscillation of the free electron density on the surface of the metal, when the metal nanocomposite is irradiated by a specific wavelength of incident light smaller than or comparable to the size of the metal.[66] The calculated adsorption energies of the Au clusters adsorbed on the (101) facet of anatase TiO_2 are given in Table 2. Compared with Ru/TiO_2, the E_{ads} of Au/TiO_2 was also negative (−0.85 eV), which indicated that the Au nanoclusters were steadily adsorbed onto the anatase TiO_2 (101) facets through chemical bonds. The interface electronic structure of the electrostatic potential and Mulliken charge were researched to investigate the effect of SPR on the intensification of the photocatalytic activity. In Table 2, the electrostatic potential of the Au/TiO_2 (101) structure (2.23 eV) was also lower than that of the (101) facet of original TiO_2 (7.033 eV). Under the formation of the Au–O–Ti chemical bond under the loaded Au clusters on the (101) facet, the final built-in

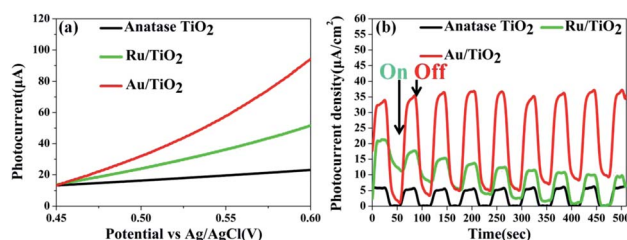Fig. 13 (a) LSV scans in Na_2SO_4 solution; (b) transient photocurrents responses of anatase TiO_2, Ru/TiO_2, and Au/TiO_2.

electric field of the Au/TiO$_2$(101) structure pointed from the Au cluster to the TiO$_2$ (101) surface layer. Also, the differences in the amount of the electron transfer from the TiO$_2$ (101) surface to the Au atoms layers indicated that the photogenerated electrons tend to localize close to the adsorbed Au clusters atoms, thus leading to the separation of the photogenerated carriers. Compared with the configuration of Ru/TiO$_2$ (101), the configuration of the Au clusters adsorbed on the (101) facet has a lower value of electrostatic potential (2.23 eV) and larger amount of transfer of Mulliken charge (2.87e), which is attributed to the effect of SPR. The final built-in electric field on the interface of Au/TiO$_2$ was enhanced due to the stronger formation of Au–O–Ti bond, exciting increase of the number of electrons on the active site of Au clusters. The formation of the local internal electric field on the interface between the Au clusters and the (101) facet of TiO$_2$ and the generation of the 'hot' electron on the surface of the Au cluster atoms when Au/TiO$_2$ was irradiated by the incident light were the effects of SPR in the application of photocatalysis.

The DOS and difference charge density of Au/TiO$_2$ are also seen in Fig. 8e and f. The electronic states of the Au 5d impurity level appeared at the top of the VB and the bottom of the CB, revealing a degree of energy dispersion. The Au clusters, their connection with the electron enrichment region of the O atoms, and the existence of an electron enrichment region around the Au clusters prove that electrons can be trapped to enrich them. However, compared with the configuration of Ru/TiO$_2$ (101), a stronger intensity of the electronic states of the Au 5d impurity level was observed (Fig. 8e) and the area of the electron enrichment region around the Au clusters increased in Au/TiO$_2$ (101) (Fig. 8f). It is indicated that the SPR effect of Au can increase the generation of electrons and intensify the final built-in electric field of the interface. The appearance of the Au 5d electronic impurity states and the formation of a new degenerate energy level synergistically narrow the band gap to increase the absorption of light.

The mechanism of the synergistic effect of electron-traps and SPR to intensify the photocatalytic overall water splitting is shown in Fig. 14. Above all, the generated electron would overcome the Schottky barrier and can be directly transfer to the surface of the electron-traps in the Au clusters as the active sites for the hydrogen evolution owing to the existence of the local final built-in electric field of the interface of the Au/TiO$_2$(101) structure that points from the Au layer to the TiO$_2$(101) surface layer and the electron enrichment region. In addition, due to the appearance of the Au 5d electronic impurity states, a set of new degenerate energy levels are formed, which narrow the band gap to increase the absorption of light. Moreover, the photo-generated 'hot' electron can be collected at the surface of the electron-traps in the Au clusters owing to the excitation of SPR on the surface of the Au cluster, leading to the enhancement in the local final built-in electric field because of the effect of SPR, when irradiated by light. Therefore, the improved utilization of the photogenerated electrons was attributed to the SPR effect that increased the number of surface electron and accelerated the migration of electrons upon deposition of Au nanoparticles on the (101) facet of anatase TiO$_2$.
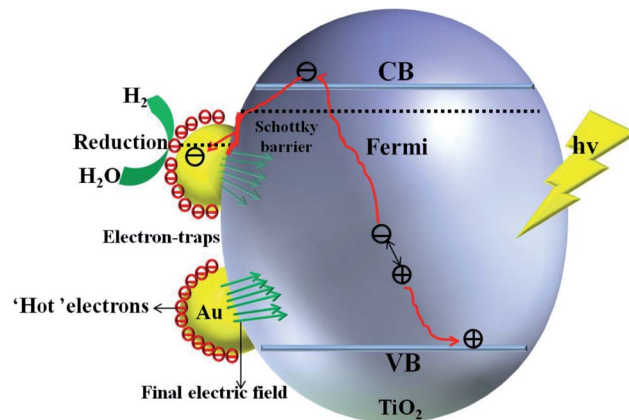

Fig. 14 Schematic illustration of mechanism of intensification of SPR.

The optical absorption of Au clusters adsorbed on TiO$_2$ displays an obvious enhancement in the visible region and obtains a smaller band gap of about 2.79 eV (Fig. 10a and b). A strong absorption at about 550 nm that emerges in the UV-Vis spectrum of Au/TiO$_2$ is attributed to the effect of SPR. Besides, the weak intensity of steady-state fluorescence was observed for Au/TiO$_2$ in the PL spectrum (Fig. 11), indicating that Au can efficiently suppress the recombination of the electron–hole pair, thus accelerating the electron transfer in the presence of the Au–O–Ti chemical bond.

Compared with the photocatalytic performance of Ru/TiO$_2$, Au/TiO$_2$ exhibits a greatly boosted evolution rate of H$_2$ (114.67 μmol g^{-1} h^{-1}), which was 2.8-fold higher than that of the Ru/TiO$_2$ photocatalyst (Fig. 12a and b). Furthermore, the stability of the Au/TiO$_2$ photocatalyst was also cycle-tested (Fig. 12d), and the amount of the H$_2$ evolution was maintained after the third cycle. Specifically, Au/TiO$_2$ showed a greatly enhanced photocurrent compared to Ru/TiO$_2$, further improving the transfer and separation of the photogenerated electron–hole pairs, which can be attributed to the effect of SPR due to the deposited Au nanoparticles (Fig. 13b).

4. Conclusions

In summary, the Ru, Au clusters deposited on the exposed (101) facet of anatase TiO$_2$ through photo-reduction route has been employed as electron-traps and active sites for HER. The greatly enhanced catalytically exposed active sites, as the electron-traps with an abundance of active sites, could efficiently promote the separation of the electron–hole pairs, assemble the photogenerated electrons, and provide active sites for the reduction reaction in photocatalytic water splitting. Compared with the electronic structure of Ru/TiO$_2$, Au/TiO$_2$ provided the plasmon-induced 'hot' electrons that can increase the generation of electrons near the surface of the Au clusters; the photogenerated electron can easily overcome the Schottky barrier and is rapidly transferred to the surface of the Au clusters under the harvesting final built-in electric field at the interface between the Au and (101) facet of TiO$_2$ owing to the SPR effect, when irradiated by light. The combined interface electronic structure

and the formation of the final built-in electric field promote the separation of the photogenerated carriers (electron–hole pairs). Besides, the appearance of the Ru 4d and Au 5d electronic impurity states, the formation of a new set of degenerate energy levels was observed, which narrows the band gap, and enhances the response and the absorption ability. In addition, Au/TiO_2 exhibits enhanced photocatalytic activity for H_2 evolution, which is attributed to the existence of synergistic effect of the electron-traps and SPR.

Conflicts of interest

The authors declare no conflict of interest.

Acknowledgements

References

1 A. Kudo and Y. Miseki, *Chem. Soc. Rev.*, 2009, **38**, 253–278.
2 B. A. Pinaud, J. D. Benck, L. C. Seitz, A. J. Forman, Z. Chen, T. G. Deutsch, B. D. James, K. N. Baum, G. N. Baum and S. Ardo, *Energy Environ. Sci.*, 2013, **6**, 1983–2002.
3 T. Takata, C. Pan and K. Domen, *Sci. Technol. Adv. Mater.*, 2015, **16**, 033506.
4 T. Hisatomi and K. Domen, *Faraday Discuss.*, 2016, **198**, 11–35.
5 Q. Wang, T. Hisatomi, Q. Jia, H. Tokudome, M. Zhong, C. Wang, Z. Pan, T. Takata, M. Nakabayashi and N. Shibata, *Nat. Mater.*, 2017, **15**, 611.
6 M. G. Kibria, F. A. Chowdhury, S. Zhao, B. Alotaibi, M. L. Trudeau, H. Guo and Z. Mi, *Nat. Commun.*, 2014, **6**, 6797.
7 R. Konta, T. Ishii, H. Kato and A. Kudo, *ChemInform*, 2004, **35**, 8992–8995.
8 T.-D. Nguyen Phan, H.-D. Pham, T. Viet Cuong, E. Jung Kim, S. Kim and E. Woo Shin, *J. Cryst. Growth*, 2009, **312**, 79–85.
9 Q. Sun and Y. Xu, *J. Phys. Chem. C*, 2010, **114**, 18911–18918.
10 C. Pan, T. Takata and K. Domen, *Chemistry*, 2016, **22**, 1854–1862.
11 W. Zhong, S. Shen, S. Feng, Z. Lin, Z. Wang and B. Fang, *CrystEngComm*, 2018, **20**, 7851–7856.
12 J. Yang, D. Wang, H. Han and C. Li, *Acc. Chem. Res.*, 2013, **46**, 1900–1909.
13 Y. W. Justin, L. Seung-Hyun Anna, M. Kazuhiko and T. E. Mallouk, *ChemInform*, 2010, **41**, 1966–1973.
14 J. Osorio-Guillén, S. Lany and A. Zunger, *Phys. Rev. Lett.*, 2008, **100**, 036601.
15 W. Zhong, S. Shen, M. He, D. Wang, Z. Wang, Z. Lin, W. Tu and J. Yu, *Appl. Catal., B*, 2019, **258**, 117967.
16 H. J. Yan, J. H. Yang, G. J. Ma, G. P. Wu, X. Zong, Z. B. Lei, J. Y. Shi and C. Li, *J. Catal.*, 2009, **266**, 165–168.
17 G. Liao, J. Fang, Q. Li, S. Li, Z. Xu and B. Fang, *Nanoscale*, 2019, **11**, 7062–7096.
18 S.-C. Yang, G. Chang, G.-J. Yang, Y.-J. Wang and B. Fang, *Catal. Sci. Technol.*, 2015, **5**, 228–233.
19 D. Xu, Q. Chu, Z. Wu, Q. Chen, S.-Q. Fan, G.-J. Yang and B. Fang, *J. Catal.*, 2015, **325**, 118–127.
20 Y.-J. Wang, G. Chang, Q. Chen, G.-J. Yang, S.-Q. Fan and B. Fang, *Chem. Commun.*, 2015, **51**, 685–688.
21 X. H. Wang, J.-G. Li, H. Kamiyama, Y. Moriyoshi and T. Ishigaki, *J. Phys. Chem. B*, 2006, **110**, 6804–6809.
22 L. Hui, C. Jian-Wen, S. Shiwei, Z. Jie, Z. Lingxia, T. Chun Kwan, C. Hua, L. Fengxia, L. Shuit-Tong and L. Yang Yang, *Small*, 2013, **9**, 37–44.
23 Y. G. Kim, J. Walker, L. A. Samuelson and J. Kumar, *Nano Lett.*, 2003, **3**, 523–525.
24 Y. Duan, N. Fu, Q. Liu, Y. Fang, X. Zhou, J. Zhang and L. Yuan, *J. Phys. Chem. C*, 2012, **116**, 8888–8893.
25 B. Grzmil, M. Glen, B. Kic and K. Lubkowski, *Ind. Eng. Chem. Res.*, 2011, **50**, 6335–6342.
26 J. Hensel, G. Wang, Y. Li and J. Z. Zhang, *Nano Lett.*, 2010, **10**, 478.
27 R. Li, Y. Weng, X. Zhou, X. Wang, Y. Mi, R. Chong, H. Han and C. Li, *Energy Environ. Sci.*, 2015, **8**, 2377–2382.
28 M. Kazuhiko, *Chem. Commun.*, 2013, **49**, 8404–8406.
29 L. K. Preethi, T. Mathews, M. Nand, S. N. Jha, C. S. Gopinath and S. Dash, *Appl. Catal., B*, 2017, **218**, 9–19.
30 H. Tada, T. Kiyonaga and S. Naya, *ChemInform*, 2009, **38**, 1849–1858.
31 H. Li, D. Wang, H. Fan, W. Ping, T. Jiang and T. Xie, *J. Colloid Interface Sci.*, 2011, **354**, 175–180.
32 H. Zhang, G. Du, W. Lu, L. Cheng, X. Zhu and J. Zheng, *CrystEngComm*, 2012, **14**, 3793–3801.
33 S. Chen, T. Takata and K. Domen, *Nat. Rev. Mater.*, 2017, **2**, 17050.
34 S. Bai, W. Yin, L. Wang, Z. Li and Y. Xiong, *RSC Adv.*, 2016, **6**, 57446–57463.
35 Z. Qiao, R. Li, L. Zheng, A. Li, S. Wang, Z. Liang, S. Liao and C. Li, *J. Catal.*, 2016, **337**, 36–44.
36 B. Ohtani, *Chem. Lett.*, 2008, **37**, 217–229.
37 P. Lei, H. Hui, C. K. Lim, Q. Y. Hong, S. T. Man and O. K. Tan, *RSC Adv.*, 2013, **3**, 3566–3571.
38 Z. Xu, Y. Hongjian, W. Guopeng, M. Guijun, W. Fuyu, W. Lu and L. Can, *J. Am. Chem. Soc.*, 2008, **130**, 7176–7177.
39 M. A. Lukowski, A. S. Daniel, C. R. English, M. Fei, A. Forticaux, R. J. Hamers and J. Song, *Energy Environ. Sci.*, 2014, **7**, 2608–2613.
40 D. Wang, R. Li, J. Zhu, J. Shi, J. Han, Z. Xu and C. Li, *J. Phys. Chem. C*, 2012, **116**, 5082–5089.
41 W. Zhong, J. Huang, S. Liang, J. Liu, Y. Li, G. Cai, Y. Jiang and J. Liu, *ACS Energy Lett.*, 2020, **5**, 31–38.
42 A. Corrado and W. Polini, *J. Manuf. Process.*, 2019, **45**, 520–531.
43 S. Sato and J. M. White, *Chem. Phys. Lett.*, 1980, **70**, 131–134.

44 Y. Liu, H. Li, W. Cen, J. Li, Z. Wang and G. Henkelman, *Phys. Chem. Chem. Phys.*, 2018, **20**, 7508–7513.

45 L. O. Paz-Borbón, F. Buendía, I. L. Garzón, A. Posada-Amarillas, F. Illas and J. Li, *Phys. Chem. Chem. Phys.*, 2019, **21**, 15286–15296.

46 J. Chen and X. Gao, *Results Phys.*, 2019, **15**, 102608.

47 G. Liao, Y. Gong, L. Zhang, H. Gao, G.-J. Yang and B. Fang, *Energy Environ. Sci.*, 2019, **12**, 2080–2147.

48 J. Ouyang, Z. Zhao, H. Yang, Y. Zhang and A. Tang, *Appl. Clay Sci.*, 2018, **152**, 221–229.

49 F. Wang, Z. Xie, J. Liang, B. Fang, Y. a. Piao, M. Hao and Z. Wang, *Environ. Sci. Technol.*, 2019, **53**, 6989–6996.

50 Q. Tang, F. Wang, X. Liu, M. Tang, Z. Zeng, J. Liang, X. Guan, J. Wang and X. Mu, *Appl. Clay Sci.*, 2016, **132–133**, 175–181.

51 A. Koichi, F. Makoto, R. Carsten, T. Junji, M. Hirotaka, O. Yoshimichi, Y. Naoya and W. Toshiya, *J. Am. Chem. Soc.*, 2008, **130**, 1676–1680.

52 M.-C. Daniel and D. Astruc, *Chem. Rev.*, 2004, **104**, 293–346.

53 B. Q. Li and L. Changhong, *Opt. Lett.*, 2011, **36**, 247.

54 H. Gao, Z. Peng, J. Zhao, J. Pan, J. Hu and G. Shao, *Appl. Catal., B*, 2017, **210**, 297–305.

55 P. Christopher, D. B. Ingram and S. Linic, *J. Phys. Chem. C*, 2010, **114**, 9173–9177.

56 L. Cano-Casanova, A. Amorós-Pérez, M. Ouzzine, M. A. Lillo-Ródenas and M. C. Román-Martínez, *Appl. Catal., B*, 2018, **220**, 645–653.

57 J. P. Perdew, *Phys. Rev. Lett.*, 1997, **78**, 3865.

58 M. D. Segall, P. J. D. Lindan, M. J. Probert, C. J. Pickard, P. J. Hasnip, S. J. Clark and M. C. Payne, *J. Phys.: Condens. Matter*, 2002, **14**, 2717–2744.

59 D. Vanderbilt, *Phys. Rev. B: Condens. Matter Mater. Phys.*, 1990, **41**, 7892.

60 B. G. Pfrommer, M. Côté, S. G. Louie and M. L. Cohen, *J. Comput. Phys.*, 1997, **131**, 233–240.

61 S. L. Dudarev, G. A. Botton, S. Y. Savrasov, C. J. Humphreys and A. P. Sutton, *Phys. Rev. B: Condens. Matter Mater. Phys.*, 1998, **57**, 1505–1509.

62 R. C. Buchanan and T. Park, *Materials crystal chemistry*, Marcel Dekker, 1997.

63 S. Mayank, W. Jun, L. Wen-Sheng, W. W. Damion, K. Seung Min, E. A. Stach, J. T. Miller, D. W. Nicholas and F. H. Ribeiro, *J. Am. Chem. Soc.*, 2012, **134**, 4700–4708.

64 H. Zhang and J. Banfield, *J. Phys. Chem. B*, 2000, **104**, 3481–3487.

65 W. Yun and G. S. Hwang, *J. Chem. Phys.*, 2005, **122**, 164706.

66 W. A. Murray and W. L. Barnes, *Adv. Mater.*, 2007, **19**, 3771–3782.